Functionalized supported membranes for quantifying adhesion of *P. falciparum*-infected erythrocytes

Benjamin Fröhlich,[1] Anil K. Dasanna,[2] Christine Lansche,[3] Julian Czajor,[1] Cecilia P. Sanchez,[3] Marek Cyrklaff,[3] Akihisa Yamamoto,[4] Alister Craig,[5] Ulrich S. Schwarz,[2,*] Michael Lanzer,[3,*] and Motomu Tanaka[1,4,*]

[1]Physical Chemistry of Biosystems, Institute of Physical Chemistry and [2]Institute for Theoretical Physics and BioQuant-Center for Quantitative Biology, Heidelberg University, Heidelberg, Germany; [3]Department of Infectious Diseases, Parasitology, Universitätsklinikum Heidelberg, Heidelberg, Germany; [4]Center for Integrative Medicine and Physics, Institute for Advanced Study, Kyoto University, Kyoto, Japan; and [5]Liverpool School of Tropical Medicine, Liverpool, United Kingdom

ABSTRACT The pathology of *Plasmodium falciparum* malaria is largely defined by the cytoadhesion of infected erythrocytes to the microvascular endothelial lining. The complexity of the endothelial surface and the large range of interactions available for the infected erythrocyte via parasite-encoded adhesins make analysis of critical contributions during cytoadherence challenging to define. Here, we have explored supported membranes functionalized with two important adhesion receptors, ICAM1 or CD36, as a quantitative biomimetic surface to help understand the processes involved in cytoadherence. Parasitized erythrocytes bound to the receptor-functionalized membranes with high efficiency and selectivity under both static and flow conditions, with infected wild-type erythrocytes displaying a higher binding capacity than do parasitized heterozygous sickle cells. We further show that the binding efficiency decreased with increasing intermolecular receptor distance and that the cell-surface contacts were highly dynamic and increased with rising wall shear stress as the cell underwent a shape transition. Computer simulations using a deformable cell model explained the wall-shear-stress-induced dynamic changes in cell shape and contact area via the specific physical properties of erythrocytes, the density of adhesins presenting knobs, and the lateral movement of receptors in the supported membrane.

SIGNIFICANCE Adhesion of infected erythrocytes to the microvascular endothelial lining is the key event that defines pathology of *Plasmodium falciparum* malaria. To dissect critical contributions involved in the complex interaction between parasitized erythrocytes and the endothelial surface, supported membranes functionalized with important adhesion receptors ICAM1 or CD36 were used as a well-defined biomimetic surface. In combination with computer simulations, our experiments revealed that the cytoadhesion of parasitized heterozygous sickle cells is reduced compared to infected wild-type erythrocytes not only because of reduced receptor-specific adhesion but also because of changes in the cell shape. Thus, our work highlights how molecular and cellular aspects synergize in the adhesion of *P. falciparum*-infected erythrocytes.

INTRODUCTION

Tropical malaria is an infectious disease caused by the unicellular eukaryotic parasite *Plasmodium falciparum*. An estimated 229 million people were infected with *P. falciparum* in 2019, of which 409,000 patients died of severe complications (1). The pathology of *P. falciparum* malaria is associated with the intraerythrocytic life cycle of the parasite. As the parasite develops within red blood cells, it changes the structure and function of the host cell (2,3). Most notably, infected erythrocytes acquire cytoadhesive properties and sequester in the deep vascular bed by adhering to the endothelial lining of microcapillaries (2,3), thus escaping clearance by the spleen. Sequestered infected erythrocytes can obstruct tissue perfusion and elicit localized inflammatory reactions, among other pathophysiological sequelae, which together contribute to severe disease.

Cytoadhesion is mediated by parasite-encoded immune-variant adhesins, of which a family of antigens, collectively termed *P. falciparum* erythrocyte membrane protein 1 (PfEMP1), plays a dominant role (2–4). PfEMP1 variants can bind to a wide range of host receptors, including receptors on the surface of endothelial cells such as CD36, intercellular adhesion molecule 1 (ICAM-1), or endothelial protein C receptor (2–4). In addition, PfEMP1 variants can mediate binding of infected erythrocytes to uninfected red blood cells, leukocytes, platelets, and serum proteins (4). Each infected erythrocyte carries ∼13,000 PfEMP1 molecules on its surface, presented in groups of three to four on parasite-induced membrane elevations, termed knobs (5). Knobs have a profound effect on the biomechanical properties of the membrane because they cause strain hardening by suppressing membrane fluctuations via increased membrane-cytoskeleton coupling (6,7).

Previous studies have shown that the sickle cell trait, which is caused by a single amino acid substitution of valine for glutamic acid at position 6 in the β-globin chain of the hemoglobin tetramer, protects carriers from severe malaria-related disease and death and that this protection is associated with altered knob morphology and a reduced cytoadhesion capability (8,9). In particular, parasitized erythrocytes containing the sickle cell hemoglobin S or related structural hemoglobinopathies present fewer and enlarged knobs (8,10), which, together with an overall reduced number of presented PfEMP1 molecules (5,9), results in a reduced ability to engage in cytoadhesive interactions. Yet, the underlying biophysical mechanisms are largely unknown.

The complexity of the endothelial surface with its multiple receptors, together with the range of interactions available to the infected erythrocyte via parasite-encoded adhesins, poses an investigative challenge and asks for a more amenable and better controllable system to define and compare critical contributions of different host receptors during cytoadhesion. Supported membranes (11,12) have been widely used to study membrane organization and receptor-ligand interactions, including cell adhesion phenomena (13–15). Because supported membranes can be fabricated from pure components, their composition can be controlled and adjusted according to experimental needs. This includes the option of functionalizing supported membranes with defined receptor proteins and varying the receptor orientation and density to represent better the variable nature of these interactions rather than the binary (binding or not binding) classification that is sometimes assumed. Given that supported membranes maintain the thermodynamic and structural properties of a free bilayer, they facilitate surface-sensitive techniques, such as cell detachment experiments via ultrasonic pressure waves to assess the intrinsic binding strengths (14,16) and reflection interference contrast microscopy (RICM) (17,18) to inform on cell-adhesive contact zones and their dynamics during shear stress or as a function of the receptor density. Thus, supported membranes offer a versatile tool to study aspects of cytoadherence that are not readily approachable in cell-cell binding assays. Despite these benefits, only one study has thus far applied the supported membrane technology to the *P. falciparum* system. By functionalizing supported membranes with chondroitin-4-sulfate (CSA), the main receptor for parasite cytoadhesion in the placenta, Rieger et al. (13) could show that binding of infected erythrocytes to CSA is cooperative, shear stress induced, and dependent on the receptor density under physiological flow conditions.

Here, we have further explored the application of supported membranes as a well-defined biomimetic surface to study quantitative aspects of cytoadhesion of *P. falciparum*-infected erythrocytes. To this end, we functionalized supported membranes with two representative host receptors presented on endothelial cells, namely CD36 and ICAM-1. We show that binding of infected erythrocytes to ICAM-1 or CD36 functionalized membranes is specific and strongly dependent on the receptor density, the mechanical loading, and the red blood cell type under both static and flow conditions. RICM revealed that the adhesion contact area of infected erythrocytes is very dynamic and defined by wall-shear-stress-induced shape transitions. We finally developed computer simulations using a deformable cell model to demonstrate that receptor redistribution due to cell shape changes explains the experimental data.

MATERIALS AND METHODS

P. falciparum culture

The *P. falciparum* IT4 (alias FCR3) strain was kept in continuous culture using HbAA and HbAS erythrocytes (19). Briefly, blood cultures were maintained at a hematocrit of 3.5% and a parasitemia not higher than 5% in Roswell Park Memorial Institute (RPMI) 1640 medium (supplemented with 2 mM L-glutamine, 25 mM HEPES, 100 μM hypoxanthine, 20 μg mL^{-1} gentamicin, and 10% (v/v) heat-inactivated human AB$^+$ serum). Cultures were kept under controlled atmospheric conditions (37°C, 3% CO$_2$, 5% O$_2$, 92% N$_2$, and 96% humidity). Binding capability to CD36 and ICAM-1 was ensured by repeatedly selecting for knobs using the gelatin flotation method (20), followed by a panning procedure over TNF-activated human dermal microvascular endothelial cells (PromoCell, Heidelberg, Germany) (21). Trophozoite stage parasites were enriched using the magnetic cell sorting method (22), yielding a parasitemia >95%. The number of infected erythrocytes was determined using a cell counter from Beckmann Coulter Diagnostics (Brea, CA).

Preparation of supported membranes

1,2-Dioleoyl-*sn*-glycero-3-phosphocholine (DOPC), 1,2-dipalmitoyl-*sn*-glycero-3-phosphocholine (DPPC), and 1,2-dioleoyl-*sn*-glycero-3-[(N-(5-amino-1-carboxypentyl)iminodiacetic acid)succinyl] (nickel salt) (DOGS-NTA (Ni^{2+})) were purchased from Avanti Polar Lipids (Alabaster, AL). Recombinant human CD36 and human ICAM-1 with histidine tags were purchased from Thermo Fisher Scientific (Waltham, MA). The glass slides (Gerhard Menzel, Braunschweig, Germany) were cleaned with the modified Radio Corporation of America (RCA) method (23), then bonded to bottomless culture dishes or to μ-Slide VI$^{0.4}$ flow chambers (ibidi, Martinsried, Germany) using polydimethylsiloxane produced from the base and the curing agent (SYLGARD184; Dow Corning, Midland, MI).

Stock solutions (5 mg mL^{-1} in CHCl$_3$) of DOPC and DOGS-NTA (Ni^{2+}) were mixed at different molar ratios χ, dried under a nitrogen stream, and stored in vacuum. The lipids were resuspended (1 mg mL^{-1}) in Hepes buffered saline (HBS) buffer (150 mM NaCl, 10 mM HEPES (pH 7.5)) and sonicated using a tip sonicater (Misonix, Farmingdale, NY), for 30 min to create small unilamellar vesicles. Residual titanium particles were removed by the centrifugation at 13,400 × g for 10 min. Supported membranes were prepared by vesicle fusion by injecting lipid suspensions into the sealed chambers for 1 h at room temperature, where supported lipid membranes are formed by vesicle fusion (11). Excess small unilamellar vesicles were removed by intensive rinsing.

Functionalization with recombinant proteins

The membranes were kept in Ni^{2+}-loaded buffer (1 mM NiCl$_2$·6H$_2$O, 150 mM NaCl, 10 mM HEPES (pH 7.5)) for 1 h to saturate NTA headgroups. After rinsing the samples with Ca^{2+}-loaded buffer (1 mM CaCl$_2$·2H$_2$O, 150 mM NaCl, 10 mM HEPES (pH 7.5)), the protein solutions (50 μg mL^{-1}) were added and incubated overnight at room temperature. Because DOPC/DPPC and DOGS-NTA (Ni^{2+}) are ideally mixed within the mixing ratios used in this study, the average interligand distance $<d>$ between CD36 or ICAM-1 can be controlled with nanometer accuracy by the fine adjustment of the molar fraction χ, assuming the lipid head area to be $A_{lipid} \sim 65$ Å^2 (24,25): $<d> = \sqrt{\frac{A_{lipid}}{\chi}}$. Before the experiments, excess proteins were removed by rinsing with RPMI-1640 (supplemented with 2 mM L-glutamine, 25 mM HEPES, 0.1% (v/v) BSA (pH 7.4)) at 37°C.

Laser-induced pressure wave assay

The critical pressure required for the cell detachment was determined by the protocol following previous accounts (13,16,26). Human erythrocytes infected with *P. falciparum* suspended in the modified RPMI-1640 medium were seeded at a cell density below 200 cells mm^{-2} and incubated for 60 min at 37°C. Thereafter, the substrate was mounted on an Eclipse Te2000-U inverted microscope (Nikon Europe, Düsseldorf, Germany) equipped with a 10×/0.40 objective and a self-built heating chamber. A laser pulse (full width at half maximum = 28 ps) generated by an Nd:YAG laser system *(λ = 1064 nm, PL2251-B-10; EKSPLA, Vilnius, Lithuania)* was focused at 0.5 mm above the substrate. The formation and collapse of a cavitation bubble induces a pressure wave propagating radially in the medium beyond the sound velocity (16,27). Before each series of measurements, we calibrated the hydrodynamic pressure P as a function of the applied laser pulse energy E_{pulse} and the radial distance r from the focal point (16). Images were taken before and after the laser pulse for different radial positions covering $r = 0$–5.7 mm. To eliminate the artifact originating from the damage caused by hot gaseous water (27), the cells found near the focal point were not included in the analysis because the theoretical maximum of the cavitation bubble size is $R \approx 1.1$ mm (28).

Dynamic adhesion and detachment of cells under shear

The dynamic adhesion and detachment of infected HbAA erythrocytes (iHbAA) and infected HbAS erythrocytes (iHbAS) under physiological shear conditions was monitored by integrating the CD36 or ICAM-1 surface into a microfluidic chamber, connected to a high precision syringe pump (Harvard Apparatus, Holliston, MA). The system was mounted onto an Axio Observer Z.1 inverted microscope (Zeiss, Oberkochen, Germany) equipped with a 40×/1.3 oil-immersion objective and an ORCA-Flash4.0 LT CMOS camera (Hamamatsu Photonics, Hamamatsu, Japan). To monitor the dynamic adhesion, the medium containing 10^6 cells mL^{-1} was injected through the chambers at different shear stresses in the range of 0.03–0.3 Pa. For each condition, the total number of attached cells

was recorded after 15 min of experiment time by taking 40 brightfield images equivalent to a total observed area of $\sim$4.4 mm^2. To examine the sustainability of cytoadhesion, the surface was first exposed to an iHbAA or iHbAS suspension at 0.03 Pa. Then, the adherent cells were exposed to the stepwise increasing shear stresses for 15 min, ranging from 0.05 to 4.0 Pa. Here, we counted the number of remaining cells for the same region of interest used for the cell adhesion ($\sim$4.4 mm^2).

Determination of cell-surface contact

The areas of adhesion contact and tight binding zone were determined by using label-free RICM as reported previously (14). The sample was illuminated with monochromatic, linear polarized light ($\lambda_{EX} = 546$ nm) through a 63×/1.25 Antiflex oil-immersion objective with a built-in λ/4 plate (Zeiss). Internal stray light is suppressed using an additional linear polarizer shifted 90° in front of the camera. To investigate the influence of shear stress on the adhesion contact and tight binding zone, 100 consecutive images with an integration time of 30 ms were collected for at least three different positions after applying a given shear stress ($\tau = 0.05$–1.0 Pa) for 10 min. The mean-square amplitude (MSA) of the light intensity was calculated for each pixel inside the projected cell contact area. The regions with MSA values below the threshold level (MSA < 0.02) were categorized as tight binding zones. The space occupied by a parasite was removed manually before analysis, as shown in Fig. 4 A.

Mesoscopic simulations

Modeling binding and detachment of infected erythrocytes in shear flow requires two key components: 1) a deformable erythrocyte model and 2) hydrodynamics. We employed multiparticle collision dynamics for hydrodynamics (29,30), combined with a widely used deformable erythrocyte model (31).

The solvent comprises N point particles with mass m, sorted in a cubic grid with side length a. The dynamics of solvent particles evolve in two steps: 1) streaming and 2) collision. For the streaming step, we have

$$r_i(t + \Delta t_{cd}) = r_i(r) + v_i(t)\Delta t_{cd}, \tag{1}$$

where Δt_{cd} is the collision time step and $v_i(t)$ is the ith particle velocity. The collision step that allows for momentum exchange among the solvent particles is

$$v_i(t + \Delta t_{cd}) = v_{cm}(t) + \mathbb{R}(\alpha)(v_i(t) - v_{cm}(t)), \tag{2}$$

where $v_{cm}(t)$ is the center of mass velocity of the grid cell to which particle i belongs and $\mathbb{R}(\alpha)$ is the stochastic rotation matrix. It is generated for each grid cell by choosing a random axis and a fixed angle α. Solvent density ρ, collision time step Δt_{cd}, and the rotation angle α determine the shear viscosity of the solvent (32).

The deformable red blood cell is modeled as two-dimensional triangular meshwork of springs with N_e edges and N_t triangles. The total potential energy is

$$V(\{x_i\}) = V_{in-plane} + V_{bend} + V_{area} + V_{volume}. \tag{3}$$

The first term is the in-plane elastic energy of the network:

$$V_{in-plane} = \sum_{j=1}^{N_e} \frac{k_B T l_m \left(3x_j^2 - 2x_j^3\right)}{4p\left(1 - x_j\right)} + \frac{k_p}{l_j}, \tag{4}$$

where the first term is the attractive worm-like chain potential and the second is the short-ranged repulsive potential, which, together, results into a spring-like potential. In an attractive potential, p is the persistence length, l_m is the maximal extension of the spring, and $x_j = l_j/l_m$.

Fröhlich et al.

The second term is the bending energy of the triangular mesh:

$$V_{\text{bend}} = \sum_{i=1}^{N_e} \kappa_b \big(1 - cos(\theta_i - \theta_0)\big), \tag{5}$$

where κ_b, θ_i, and θ_0 are the bending modulus, the angle between the two faces sharing the same edge, and the preferred angle, respectively.

The last two terms in Eq. 3 correspond to surface area and volume constraints:

$$V_{\text{area}} = \frac{k_a(A - A_0)^2}{2A_0} + \sum_{j}^{N_t} \frac{k_d\left(A_j - A_j^0\right)^2}{2A_j^0} \tag{6}$$

and

$$V_{\text{volume}} = \frac{k_d(V - V_0)^2}{2V_0}, \tag{7}$$

where k_a and k_d are global area and local area constrain coefficients and k_v is the volume constraint coefficient. All the three coefficients were chosen such that the membrane is nearly incompressible and that the total surface and volume fluctuate within 1% throughout the simulation. For a perfectly hexagonal network, an in-plane elastic modulus, such as a shear or Young's modulus, depends on the choice of model parameters. The shape of the infected cell is chosen to be a discocyte because the trophozoite stage cell is known to have almost retained its initial discocyte shape. The drastic changes in shape start to occur 24–30 h postinvasion (33). The mass of the membrane vertex is set to ρm. The size of an erythrocyte is chosen to be $D_0 \sim \sqrt{A/\pi}$, and the mean edge length is close to $0.5a$. The coupling between solvent particles and membrane vertices is introduced via two ways: 1) membrane vertices are included in the collision scheme and 2) solvent particles bounce back at the triangular plaquettes, separating the inside and the outside fluid. The solvent particle density is chosen to be $\rho = 12\frac{m}{a^3}$ and $dt_{cd} = 0.01\sqrt{ma^2/k_BT}$, which results in the viscosity $\eta = 104\frac{\sqrt{mk_BT}}{a^2}$. For a typical shear rate of $\dot{\gamma} = 0.1$, the Reynolds number becomes $Re = R^2\dot{\gamma}\rho/\eta \sim 0.18 < 1$. Model units to physical units can be converted by equating the relevant length, force, and timescales (31). For example, the erythrocyte diameter in simulations sets the length scale, i.e., $7.8a$ is equivalent to 6.5 μm, which makes $a \approx 0.82$ μm. Simulation time is approximated with physical time by matching the relaxation time, $\tau = \frac{\eta D_0^3}{\kappa_b}$. The shear modulus of both iHbAA and iHbAS cells is set to 25 μN/m, taking the value measured by optical tweezers (34). The bending modulus for iHbAA cells is set to 4.1×10^{-19} J, and for iHbAS, it is 5.6×10^{-19} J, as determined by flicker spectroscopy (6).

Bond dynamics are employed between the membrane vertices (which also act as receptors) and the ligands that are uniformly distributed on the substrate. The choice of knobs is done using a random procedure which ensures that each trajectory is made with a different knob configuration. At each integration time step dt_{md}, possible bond associations and bond dissociations are performed among vacant receptors and vacant ligands. For bond association, the receptor forms a bond with an available ligand if the distance is less than a critical distance $r_0 = 0.375a$ with a constant on rate κ_{on}. The on rate is chosen in the range of 10–1000 s^{-1}. For bond dissociation, we have employed Bell's model (35), in which the off rate depends on the force $\kappa_{off} = \kappa_{off}^0 e^{\left(\frac{F}{F_d}\right)}$, where F_d is the internal bond force scale, which is close to 10 pN for the PfEMP-1:CD36 bond (36). The unstressed off rate is chosen in the range of 1–10 s^{-1}. We modeled the receptor-ligand bond with a cable force model (37,38): $F(l) = k_s(l - l_0)$ when l is greater than l_0, else zero, where $k_s \approx 2$ μN/m and $l_0 = 0.15a$. At each step, the probabilities for bond association and bond dissociation are computed to be $P_{on} = 1 - \exp(-\kappa_{on}\Delta t_{md})$ and $P_{off} = 1 - \exp(-\kappa_{off}\Delta t_{md})$, respectively, and the unstressed off rate is chosen to be 10 s^{-1}.

For measuring binding events, we employed Stokesian dynamics of spherical particle in shear flow to avoid extensive computational complexity. The details of the algorithm are laid out in (37,38). Here, we avoid using bond dynamics as we assume that when the cell reaches close to the substrate (less than 50 nm), it would bind to the substrate, which is a fair assumption because the density of ligands on the substrate is very high.

Computer simulations setup

All flow simulations are performed in a three-dimensional rectangular box of the size $36a \times 20a \times 20a$. Periodic boundary conditions are employed along the x and y directions, whereas hard wall boundary conditions are employed in the z direction. Solvent particles make bounce-back collisions with hard walls, but this is not sufficient to account for the no-slip boundary condition at the walls, which is resolved by adding ghost particles in grid cells that are cut by the walls (39). Shear flow $\mathbf{v} = \dot{\gamma}z\mathbf{e}_x$ is employed along the x direction. Shear flow is generated by adding an offset velocity v_{wall} to the ghost particles that reside in the grid cells that are cut by the wall at $z = L_z$, which generates shear flow with shear rate $\dot{\gamma} = v_{wall}/L_z$. Before starting the flow, we place the cell close to the substrate and let it adhere until it reaches the steady state, and then after, we initiate the flow.

Statistics

The presented data were obtained from three independent experiments using blood from more than two different donors both for iHbAA and iHbAS erythrocytes. If not stated otherwise, the data points and error bars represent mean values and standard deviations, respectively.

Ethical clearance

The experiments were approved by the ethics review board of Heidelberg University and Mannheim University. The experiments were performed after obtaining informed consent from all voluntary donors in accordance with the relevant guidelines and regulations.

RESULTS

Detachment of adherent cells depends on receptor density and red blood cell type

Throughout the study, we used the *P. falciparum* strain IT4 (alias FCR3), which was repeatedly panned over primary human dermal microvascular endothelial cells to enrich for parasite populations adhering to two representative host receptors on the surface of endothelial cells, namely CD36 and ICAM-1, before the experiments. A detailed transcriptional analysis revealed predominant expression of the three PfEMP1 encoding var genes, *IT4var13*, *IT4var25*, and *IT4var66* (40). These var genes belong to the subtypes UpsB and UpsC and are predicted to encode ICAM-1 and/or CD36 binding PfEMP1 variants (41).

We first determined the adhesion strength of *P. falciparum*-infected erythrocytes at the trophozoite stage (24–32 h postinvasion) on supported membranes (12–14) displaying CD36 or ICAM-1 at different densities (Fig. 1 A), using an ultrasonic pressure wave generated by a picosecond laser pulse (Fig. 1 B; (13,16)). Before the experiments, we confirmed that the nonspecific adhesion of uninfected erythrocytes to membranes displaying CD36/ICAM-1 is negligibly small
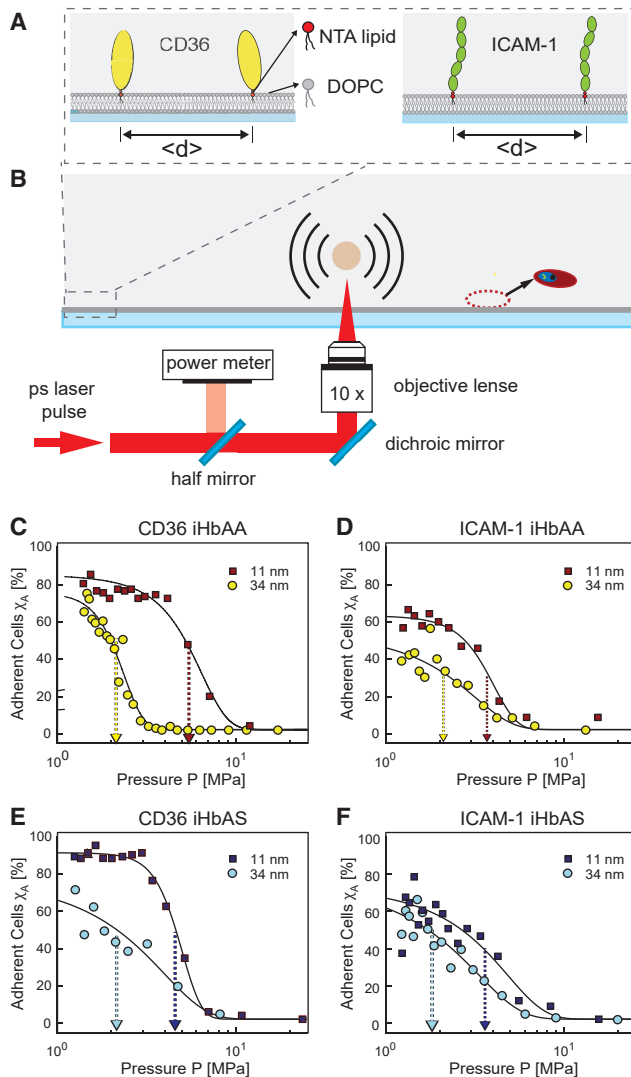
FIGURE 1 (A) Schematic illustration of the functionalized surfaces based on planar lipid membranes. The supported membranes were functionalized by selectively coupling recombinant CD36 and ICAM-1, each carrying a histidine tag, via a nitrilotriacetic acid (NTA) headgroup to anchor lipids. $<d>$, mean inter-receptor distance. (B) Experimental setup to quantify the adhesion strength of infected erythrocytes HbAA (iHbAA) and HbAS (iHbAS) erythrocytes, using a pressure wave induced by a picosecond laser pulse focused 0.5 mm above the substrate. (C–F) Fraction of remaining cells normalized by the number of initially adherent cells χ_A plotted as a function of pressure exerted on cells. (C) iHbAA on CD36, (D) iHbAA on ICAM-1, (E) iHbAS on CD36, and (F) iHbAS on ICAM-1. Arrows indicate the critical pressure to detach prebound cells P^*. Each data point represents the mean of 50 individual cells. To see this figure in color, go online.

(Fig. S1). Because the ultrasonic pressure wave interacts with the cells for only ~80 ns but at MPa strength, the cellular response is purely elastic. Because of the noninvasive nature of this technique, cells remain viable during the course of the experiment and are able to readhere after detachment.

Because the ultrasonic pressure exerted on cells depends on the radial distance from the initial focus point r_{Focus}

(Fig. S2), the experimentally obtained fraction of adherent cells remaining on the surface normalized by the number of initially adherent cells χ_A can be analyzed as a function of the radial distance and, hence, the local pressure P. The obtained χ_A-P relationship can be fitted with an error function:

$$\chi_A(P) = \frac{\chi_0}{2}\left(1 - \mathrm{erf}\left(\frac{P - P^*}{\sqrt{2}\sigma}\right)\right). \qquad (8)$$

χ_0 is the initial level, and P^* and σ are the critical pressure and its standard deviation corresponding to the transition from the adherent to the detached state.

We found that the critical pressure to detach prebound cells declined with increasing intermolecular receptor distances $<d>$ (Fig. 1, C and D). For instance, the P^*-values (indicated by *arrows* in Fig. 1, C–F) decreased more than twofold, from 5.6 to 2.2 MPa, as the intermolecular CD36 distance increased from 11 to 34 nm. Similarly, P^* declined from 3.6 to 2.1 MPa as the intermolecular distance of ICAM-1 increased from 11 to 34 nm. Infected HbAS erythrocytes revealed a detachment behavior on CD36- and ICAM-1-functionalized surfaces qualitatively similar to that of parasitized HbAA red blood cells, albeit the curves were shifted to lower pressure values (Fig. 1, E and F; see also Fig. S3, A and B for an extended $<d>$ range), which was also suggested by previous reports (8,10,40). We further noted that both iHbAA and iHbAS exhibited sharper transitions from the adherent to the detached state on CD36 compared with ICAM-1.

Dynamic binding of infected erythrocytes under shear stress

We next investigated the dynamic aspects of adhesion under physiological hydrodynamic shear stress, using a microfluidic device (Fig. 2 A). The number of bound cells N_B was determined for each condition and normalized by unit area (mm^2) and volume of applied blood suspension (milliliters) to allow for the direct comparison of data collected at different volume fluxes.

Fig. 2 B shows the number of bound cells N_B [mL^{-1} mm^{-2}] for iHbAA and iHbAS erythrocytes to surfaces functionalized with CD36 at $<d>_{CD36} = 11$ nm, plotted as a function of shear stress τ. The number of binding events gradually decreased with increasing shear stress. For example, the binding of infected HbAA erythrocytes decreased by one order of magnitude from $\Delta N_{iHbAA/CD36} = 185$ to 15 mL^{-1} mm^{-2} as the shear stress increased from $\tau = 0.03$ to 0.10 Pa. Similar to our results with the pressure wave assay, infected HbAS erythrocytes exhibited the same tendency, albeit at an overall lower binding capacity. For example, the number of binding events at $\tau = 0.03$ Pa, $\Delta N_{iHbAS/CD36} = 117$ mL^{-1} mm^{-2}, was reduced by ~30% as compared with parasitized wild-type red erythrocytes.
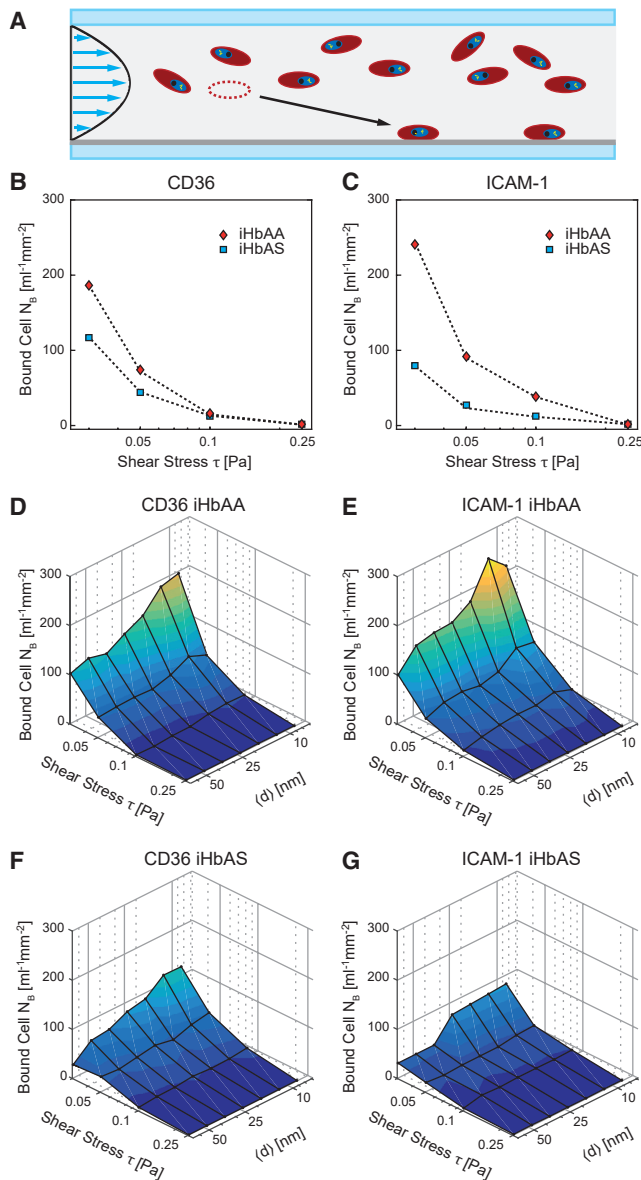
FIGURE 2 (*A*) Schematic illustration of the microfluidic setup to observe dynamic adhesion of infected erythrocytes under conditions of shear stress. The number of bound cells N_B of infected HbAA (iHbAA, *red*) and HbAS (iHbAS, *blue*) erythrocytes to the surfaces displaying (*B*) CD36 and (*C*) ICAM-1 at $<d> = 11$ nm is shown. The number of bound cells N_B of infected HbAA and HbAS erythrocytes on (*D* and *F*) CD36 and (*E* and *G*) ICAM-1, plotted as functions of shear stress τ and $<d>$, is shown. To see this figure in color, go online.

Comparable results were obtained for ICAM-1 (Fig. 2 *C*). Again, the number of binding events decreased with increasing shear stress for both infected HbAA and HbAS erythrocytes. However, there were some distinctions with regard to the results obtained on CD36-functionalized membranes. More infected HbAA erythrocytes bound to ICAM-1 than to CD36 under comparable conditions ($\Delta N_{iHbAA/ICAM-1} = 245$ mL^{-1} mm^{-2} at $\tau = 0.03$ Pa), and the differences in binding capacity between infected

HbAA and HbAS erythrocytes were more pronounced in the case of ICAM-1 than of CD36 ($\Delta N_{iHbAS/ICAM-1} = 79$ mL^{-1} mm^{-2} obtained at $\tau = 0.03$ Pa).

To assess the effect of receptor density on cytoadhesion, we performed flow experiments under systematic variation of $<d>$ from 6 to 67 nm (Fig. 2, *D and E*). In the case of CD36 (Fig. 2 *D*), the binding of infected HbAA erythrocytes monotonically decreased with increasing τ and increasing $<d>$ but did not reach zero at the largest interligand distance $<d> = 67$ nm and $\tau = 0.03$ Pa, possibly because of lateral diffusion and accumulation of receptors on the surface of supported membranes retaining their intrinsic lateral fluidity. In the case of ICAM-1 (Fig. 2 *E*), the number of bound cells first rose to a maximum as $<d>$ increased before it fell to a basal value. This phenomenon was particularly evident at lower wall shear stresses. In the case of infected HbAS erythrocytes, the number of cells bound to CD36 (Fig. 2 *F*) and ICAM-1 (Fig. 2 *G*) was distinctly lower compared with wild-type HbAA erythrocytes. Uninfected red blood cells did not bind to the supported membranes at any of the conditions tested, excluding the possibility of nonspecific cell adhesion (Fig. S1).

Persistence of cytoadhesion under shear

We next investigated the cytoadhesion strength of prebound cells under increasing wall shear stress. To this end, infected erythrocytes at a hematocrit of 10^6 cells mL^{-1} were flushed over CD36 or ICAM-1 functionalized membranes for 15 min at a low wall shear stress ($\tau = 0.03$ Pa). The shear stress was then increased from 0.05 to 4.0 Pa in a stepwise manner, covering the physiological range (Fig. 3 *A*; (42)). Fig. 3, *B–E* depict the surface density of infected HbAA erythrocytes N_R [mm^{-2}] remaining attached to CD36 and ICAM-1, respectively, as a function of the shear stress τ. Sigmoidal relationships emerged for both intermolecular distances investigated ($<d> = 11$ and 34 nm) and for both parasitized HbAA and HbAS red blood cells. However, there were consistently fewer cells attached at an intermolecular distance of 34 nm than at 11 nm, and infected HbAS erythrocytes displayed two- to threefold lower N_R-values under all experimental conditions. It is worth pointing out that the majority of remaining cells could resist hydrodynamic pressures of up to 0.5 Pa, suggesting that cytoadhesion is persistent once bond formation has been established.

To compare the sustainability of cytoadhesion in flow quantitatively, each data set was fitted with an error function (*solid lines* in Fig. 3, *B–E*),

$$N_R(\tau) = \frac{N_R^0}{2}\left(-\text{erf}\left(\frac{\tau - \tau^*}{\sqrt{2}\sigma}\right) + 1\right), \quad (9)$$

yielding the critical shear stress for the cell detachment τ^*. On surfaces displaying CD36 at $<d> = 11$ nm (Fig. 3, *B*
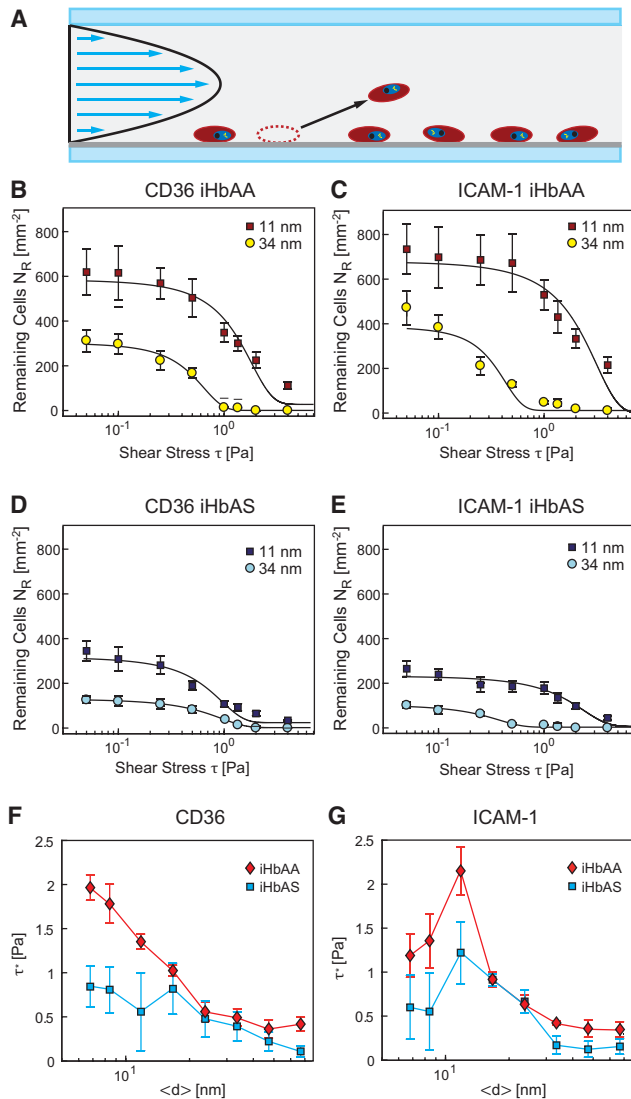
FIGURE 3 (A) Detachment of adherent cells by stepwise increasing the applied shear stress τ. Surface density of remaining iHbAA erythrocytes N_R on (B) CD36 and (C) ICAM-1 surfaces is plotted as a function of shear stress τ. Experiments were performed at $<d> = 11$ nm (*squares*) and 34 nm (*circles*). The corresponding data of iHbAS erythrocytes are presented in (D) and (E). Critical shear stress of detachment τ^* on (F) CD36 and (G) ICAM-1 surfaces, plotted as a function of $<d>$, is shown. To see this figure in color, go online.

and D), the critical shear stress for the detachment of infected HbAA and HbAS erythrocytes was 1.35 and 0.56 Pa, respectively. In the case of ICAM-1 with $<d> = 11$ nm (Fig. 3, C and E), τ^*-values of 2.2 and 1.2 Pa were obtained for infected HbAA and HbAS erythrocytes, respectively. Overall, these data quantitatively demonstrate that iHbAS erythrocytes are strongly impaired in maintaining cytoadhesion, as qualitatively suggested by previous reports (8,10,40).

To better assess the effect of the intermolecular receptor distance on cell detachment, we extended our study to include six additional $<d>$-values (spanning a $<d>$-range from 6 to

67 nm) and then quantified the data using the error function described above (Eq. 9), yielding τ^* as a function of the intermolecular receptor distance. As seen in Fig. 3 F, τ^* decreased in a monotonic manner with increasing CD36 intermolecular distance for both infected erythrocyte variants. In comparison, for ICAM-1, τ^* rose to a maximum at $<d>$ of 11 nm before it fell with increasing intermolecular distances. The observed phenotypic difference suggests the presence of an optimal arrangement of ICAM-1 to sustain the cytoadhesion of infected erythrocytes. As this phenomenon was observed for both infected HbAA and HbAS erythrocytes, it does not correlate with the size and density of knobs. Conversely, the monotonic decrease in τ^* observed on CD36 surfaces indicates that there is no optimal arrangement for CD36, either for infected wild-type or sickle trait erythrocytes.

Changes in cell shape and cell-substrate contact by shear

Cells exposed to shear stresses undergo viscoelastic deformation and adapt their adhesion contacts (43). These cellular factors might be equally important as molecular ones, especially when considering the persistence of cytoadhesion after the establishment of initial adhesion. Extending our ensemble observation of cell adhesion and detachment, we monitored changes in the cell-surface contacts caused by shear stresses ($\tau = 0.05–1.0$ Pa), using RICM. As the intensity of light detected at each pixel reflects the separation distance between the cell membrane and the substrate, we categorized two regions as follows (Fig. 4): 1) the adhesion contact area as defined by calculating the gradient of the time average of $100\times$ RICM images (regions surrounded by *purple solid lines*) and 2) the tight binding zone as identified by thresholding the MSA of intensity and distance fluctuation at MSA < 0.02 (regions shaded in *dark gray*).

The left row of Fig. 4 A depicts the RICM images (*left*) and the extracted cell-surface contacts (*right*) of infected HbAA erythrocytes on a CD36 surface ($<d> = 11$ nm) at $\tau = 0.10, 0.25$, and 1.0 Pa. The red arrow indicates the direction of flow. The adhesion contact area increased with rising shear stress. At $\tau = 0.10$ Pa, the adhesion contact area resembled a "U shape," with no adhesion contact on the side facing the flow. When the shear stress was increased to $\tau = 0.25$ Pa, the opening closed, and the adhesion contact zone adopted an "O shape." Concomitant with the changes in contact area, the cells altered their morphology as τ increased. At low τ, the cells sustained discocyte-like shapes. No adhesion contact was established in the middle of the cell. Once the shear stress reached $\tau = 1.0$ Pa, the cell and the adhesion contact area took on a "raindrop shape," indicating that the tip of the cell facing the flow was pinned. We note that these shape transformations were driven by shear flow.

Infected HbAS erythrocytes exhibited qualitatively similar changes in response to increasing shear stress. To
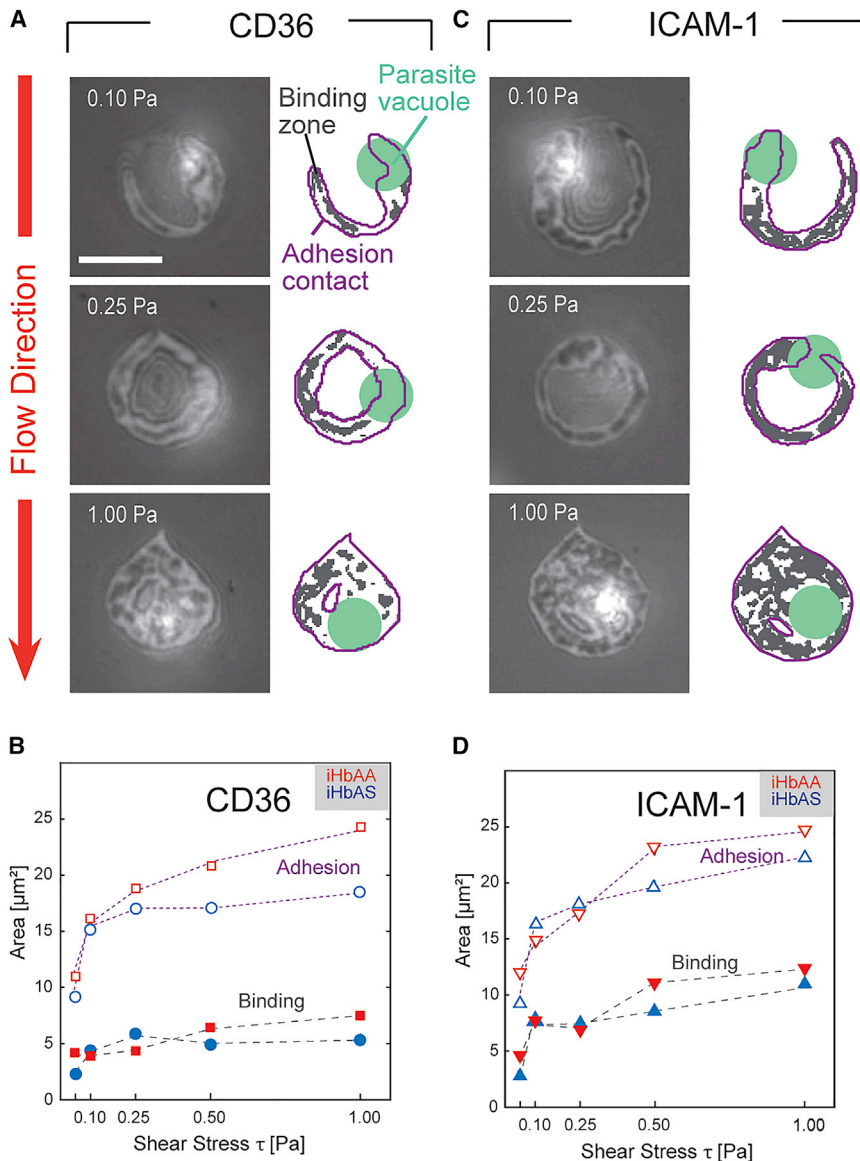
FIGURE 4 (*A*) Left: RICM images of an iHbAA erythrocyte on a surface displaying CD36 at $<d> = 11$ nm with increasing shear stress. Scale bars, 5 μm. A red arrow indicates the flow direction. Right: Adhesion contacts (surrounded by *purple solid line*), tight binding zones (*shaded in dark gray*), and parasite vacuoles (*shaded in green*) extracted from the corresponding RICM images. (*B*) Areas of adhesion contact (*open symbols*) and tight binding zone (*solid symbols*) of iHbAA (*red*) and iHbAS (*blue*) plotted as a function of shear stress τ. The corresponding data sets on ICAM-1 surfaces are presented in (*C*) and (*D*). To see this figure in color, go online.

highlight the difference between infected HbAA and HbAS erythrocytes, the contact area and the tight binding zone were plotted as a function of the shear stress (Fig. 4 *B*). The contact area of infected HbAA erythrocytes increased from 11 to 25 μm^2 as the shear stress rose from $\tau = 0.05–1.00$ Pa, respectively. The contact area of infected HbAS erythrocytes initially exhibited a similar increase up to 17 μm^2, but there was no further increase at $\tau \geq 0.25$ Pa. It should be noted that changes in the binding zones of both infected HbAA and HbAS erythrocytes were less dependent on shear stress, suggesting that the unbinding from CD36 bond is not shear dependent. This finding agrees with the data presented in Fig. 3 *F*.

As presented in Fig. 4 *C*, the adhesion contact area of an infected HbAA erythrocyte on ICAM-1 surfaces also underwent the shape transition from a U through an O to a rain-

drop shape, and concomitantly, the adhesion contact area grew from 11 to 25 μm^2 (Fig. 4 *D*) with increasing shear stress from 0.05 to 1.00 Pa. This finding is comparable to that made on CD36 surfaces (Fig. 4 *B*), with the exception that the ICAM-1 tight binding zone exhibited a remarkable increase from 4 to 12 μm^2 with increasing shear stress, which was not seen to the same extent on CD36 surfaces. A statistical analysis confirmed that the sizes of the tight binding zones were statistically different between ICAM-1 and CD36 surfaces at 1.00 Pa (12 vs. 5.6 μm^2, respectively; χ^2 test, $p = 0.01$), although the starting values at 0.05 Pa were comparable. As shown in Fig. 4 *D*, infected HbAS erythrocytes exhibited a qualitatively similar shear-induced adhesion behavior. The contact area and binding zone quickly increased after a rise in shear stress from 0.05 to 0.10 Pa. At $\tau \geq 0.25$ Pa, the gains in adhesion became
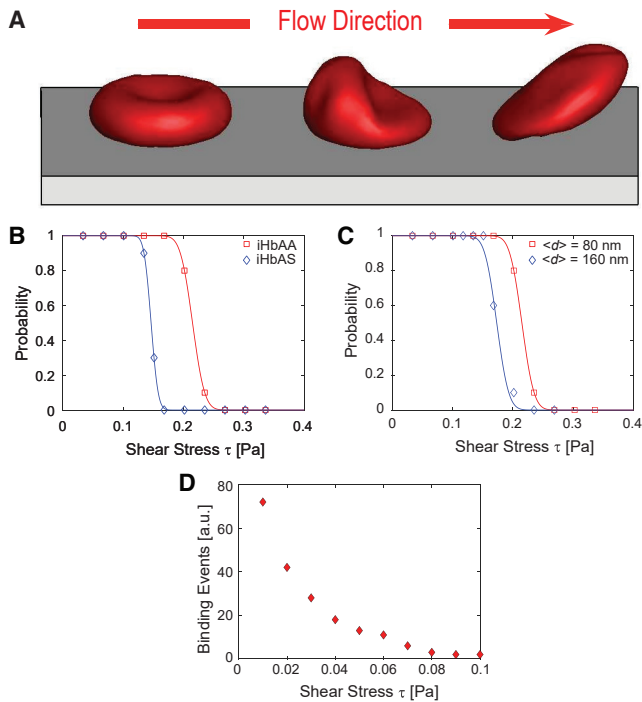
FIGURE 5 (*A*) Computer simulations with deformable cell model for an adhered erythrocyte moving over the substrate under shear flow. A red arrow indicates the flow direction. (*B*) The probability of an iHbAA and iHbAS erythrocyte to sustain adhesion on surfaces with at $<d> = 80$ nm under shear. (*C*) The probability of an iHbAA erythrocyte to sustain adhesion under shear at $<d> = 80$ nm and $<d> = 160$ nm. Values for knob density, shear modulus, and bending modulus of iHbAA and iHbAS erythrocytes were included in the simulation and were taken from our previous accounts (6,40). (*D*) The number of binding events, simulated for a spherical particle in shear flow using Stokesian dynamics, is plotted against shear stress. To see this figure in color, go online.

smaller. The increase in the size of the tight binding zone on ICAM-1 surfaces indicated a shear-induced, lateral accumulation of ICAM-1 owing to the fluid nature of supported membranes. Intriguingly, on CD36 surfaces, the binding zone exhibited a similar shape transition but showed no remarkable change in size. Previously, it has been reported that both CD36 and ICAM-1 form clusters in the region of cell-cell contacts (44,45). However, the differential lateral reorganization between ICAM-1 and CD36 could be identified only by using precisely functionalized, fluid supported membranes.

Assessing shear-induced cell deformations by mesoscopic computer simulations

Recently, mesoscopic computer simulations have been established as an instructive method to interpret results from quantitative flow chamber experiments (37,40). Using triangulated surfaces for cell shape and multiparticle collision dynamics for hydrodynamic flow, one can simulate how adherent cells deform and move on a substrate (Fig. 5 *A*). However, these kinds of simulations are very time consuming. If shape changes are not the main focus, one can use Stokesian dynamics simulations of spherical particles in shear flow to get better statistics. Here, we used both approaches to simulate the effect of shear flow and receptor distance on the cytoadhesion of iHbAA and iHbAS cells. We first used the deformable cell model. To reflect the naturally occurring variability in knob density, we have used a range within which we varied the knob density instead of fixing it. We used 6–8 knobs μm^{-2} for iHbAA and 3–5 knobs μm^{-2} for iHbAS (40). For each realization, we chose the number of active vertices randomly within a range that corresponds to the respective knob density range. In Fig. 5, *B and C*, we show the probabilities of the cells to adhere against the shear stress τ as a function of ligand distance and hemoglobin variant, respectively. Each point for a given shear stress is an average of 10 different simulations performed, and for each realization, the knob density is chosen randomly. The probability is simply given by the ratio of number of realizations when the cell survived to the total number of realizations. The critical shear stress for the binding-unbinding transition determined with the error function is 0.22 and 0.15 Pa for iHbAA and iHbAS, respectively. The values are reasonably close to the experimental values (see Fig. 3, *F and G*).

To estimate the binding events and its dependence on shear stress, we used Stokesian dynamics simulations. For each shear stress, we run multiple simulations with different initial heights (up to 25 μm), and we counted how many cells fall close to 50 nm to the substrate without exceeding 5 mm along the flow direction. This simulation setup is designed to imitate the binding events measurements in the flow chamber experiments described above. The results are not sensitive to the cutoff distances. In Fig. 5 *D*, we show the number of cells that succeed in making contact with the substrate for varying shear stress. The dependence agrees well with Fig. 2 *A*. Because no bond dynamics is employed, we captured the phenomenon qualitatively, but not quantitatively. We conclude that the difference between binding events of iHbAA and iHbAS in experiments is mainly due to differences in knob density.

Our computer simulations with deformable cells can also shed light on the contact zone with the substrate and its dynamic changes under the shear. Fig. 6 *A* represents the side view (*upper panels*) and the bottom view (*lower panels*) of an infected erythrocyte undergoing a shear-induced deformation simulated by mesoscopic computer simulations. The gray scale represents the absolute mean curvature. The adhesion contacts, surrounded by solid black lines in the lower panels, exhibit a transition from a U shape to an O shape, which reproduces the experimental results (Fig. 4, *A and C*). In Fig. 6, *B and C*, we show the change in the adhesion contact area for both iHbAA and iHbAS cells. iHbAA cells show a monotonic increase, and iHbAS cells are less prominent than iHbAA, which is due to relatively small knob density. These results agree well with
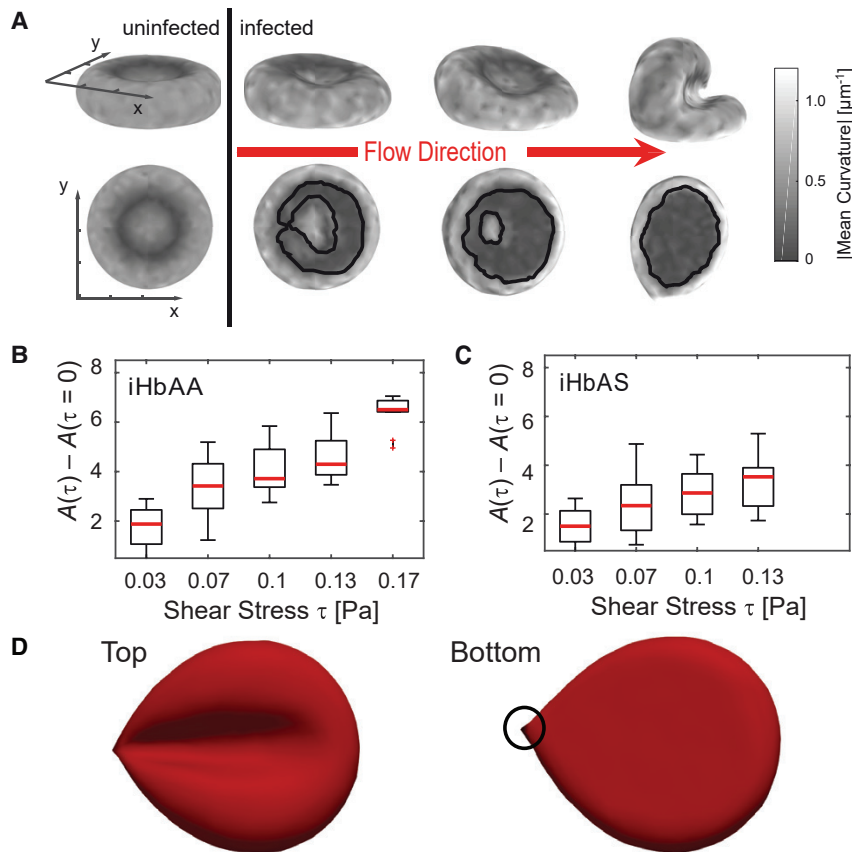
FIGURE 6 (*A*) Side (*upper row*) and bottom (*lower rows*) views of an infected erythrocyte simulated with the deformable cell model under different shear conditions. The regions surrounded by solid black lines coincide with adhesion contacts. (*B*) Change in contact area under varying shear stress for iHbAA cells; the same is displayed for (*C*) iHbAS cells. For both (*B*) and (*C*), the interligand distance is $<d> = 80$ nm. (*D*) Snapshots (*left*: *top view*, *right*: *bottom view*) of adherent iHbAA cells under high shear stress flows. The shear flow direction is from left to right. The circle on the bottom viewed snapshot indicates the position of strongly adhered knob. The strong adhesion contact or knob is modeled with higher spring constant and multiple receptors rather than one receptor per knob as in default case. The shear stress is $\tau \approx 0.5$ Pa. To see this figure in color, go online.

the experiments (Fig. 4, *B and D*). It should be noted that the change in area given in μm^2 is only a semiquantitative indicator because the adhesion contact area strongly depends on how the adhesion contact is defined. In simulations, we measured the contact area as the membrane surface that is bonded with the substrate. Thus, this would be equivalent to the binding area in experimental measurements.

At the highest shear, the adhesion contact became homogeneous. We noted that the experimentally observed sharp tip of the raindrop shapes cannot be reproduced with homogeneous coverage of knobs. We speculate that such sharp tips are the result of an accumulation of receptors moving in the supported membranes, resulting in a few strong adhesion contacts that hold the entire cell. When the supported membrane consists of lipids in fluid phase, the lipids, as well as recombinant proteins coupled to anchor lipids, undergo free lateral diffusion (46). In our previous account, we showed that the kinetics of cancer cell apoptosis driven by the ligand-receptor pairs becomes distinctly slower when the recombinant proteins were anchored on a membrane in a gel phase (15). To recapitulate the effect caused by the accumulation of receptors, we modeled the cell with few strong adhesions and many weak adhesions. For strong adhesions, more than one receptor is used per knob, and the bond strength is increased by a factor of 10. In Fig. 6 *D*, we show cell snapshots (both *top view* and *bottom view*) for a

cell with one strong adhesion along with few hundreds of weak adhesions. The sharp tip appeared on the front side of the cell. It resembles the cell snapshots from Fig. 4, *A and C* at higher shear stress. We also simulated cells with a higher number of strong adhesions, resulting in conformations with multiple sharp edges. These simulations were performed at shear stress $\tau = 0.5$ Pa, and on and off rates were chosen such that the cells do not detach from the substrate. Some of the features of the raindrop shape could also be seen in recent simulations when the cell has very few adhesion contacts (47).

To further verify our hypothesis, we compared the shape of adhesion contacts on 1,2-palmitoyl-*sn*-glycero-3-phosphocholine (DPPC) membranes in gel phase, displaying CD36 and ICAM-1 at $<d> = 11$ nm. As presented in Fig. S5, the adhesion contact did not take a raindrop shape even at the highest shear (1.00 Pa). This result indicates that the fluidity of supported membranes, which shares a common feature with the plasma membrane of endothelial cells, allows for the lateral accumulation of ligand-receptor pairs, resulting in the strong pinning near the tip of the cell facing to the flow. The capability of supported membranes to control both inter-receptor distance and membrane fluidity helped us unravel how the individual molecular interactions manifest themselves on the cellular level.

DISCUSSION

Our study suggests that receptor-functionalized supported membranes are a valuable complementary tool to study the processes underpinning cytoadherence of *P. falciparum*-infected erythrocytes. Unlike microvascular endothelial cells, which can present multiple cytoadhesion receptors at variable density and distribution on their surface (48–51) in a manner affected by the activation state (52,53), supported membranes offer the option of controlling the receptor identity, orientation, and density. Thus, cytoadhesion studies can be performed under controlled conditions, providing additional insights into the dynamics and kinetics of cytoadherence, which are not easily acquirable by using microvascular endothelial cells or receptor-coated petri dishes.

Previous studies using microvascular endothelial cells have shown that the number of adhering infected erythrocytes and their adhesion strength increase with the receptor density (48–51). Our study now provides a quantitative understanding of this observation by revealing that adhesion parameters declined with increasing receptor distance over a range of 10–∼100 nm for both CD36 and ICAM-1 at all wall shear stresses investigated. The red blood cell type, the knob density, and the amount and type of PfEMP1 variant presented on the cell surface are variables that can affect this relationship (see below for further discussion).

According to Sanchez et al., each knob carries on average three to four PfEMP1 molecules placed 18–14 nm apart from one another at the tip of the knob, as shown for the PfEMP1 variant VAR2CSA that confers binding of infected erythrocytes to placental CSA (5). Interestingly, the receptor distance supporting optimal cytoadhesion seems to be in the same nanometer range. Whether the spatial arrangement of PfEMP1 molecules on knobs has evolved to match the spacing of receptor molecules and hence to support efficient cytoadherence or whether these are two coincidental events will require further investigation. Further studies would also be needed to investigate whether the positioning of VAR2-CSA on knobs is a general property of other PfEMP1 variants.

Supported membranes further allowed us to assess dynamics in contact footprint using RICM. In flow chamber experiments, infected erythrocytes respond to external shear stresses by adapting their shape before the hydrodynamic pressure peels them off from the surface once the wall shear stress exceeds a critical value. We now observed that the morphological changes induced by shear profoundly affected the contact footprint between the cell and the substrate, in that the contact area grew in size (from 11 to 25 μm^2) as the wall shear stress increased. Moreover, the contact area changed its form—from "U shaped" ($\tau = 0.10$ Pa) to "O shaped" ($\tau = 0.25$ Pa) to "raindrop shaped" ($\tau = 1.0$ Pa). In addition, the tight binding zone increased at least for ICAM-1 surfaces (from 4 μm^2 at $\tau = 0.05$ Pa to 12 μm^2 at $\tau = 1.0$ Pa) but remained almost constant on CD36 surfaces (5.6 μm^2 at $\tau = 1.0$ Pa).

The increase in contact area and tight binding zone with increasing flow seems counterintuitive. However, our mesoscopic computer simulations explain this behavior by the specific cellular and biomechanical properties of the infected erythrocyte, including membrane mechanics and knob density (6,40), and the lateral recruitment and accumulation of receptors at sites of contact. In other words, the shape transition and the gain in contact area under conditions of increasing wall shear stress are ascribed to the ability of infected erythrocytes to respond to hydrodynamic pressure with changes in cell shape, which, in turn, increases the cell-surface area that can interact with the support. The ability to engage in binding events then depends on the knob density and the intermolecular receptor distance, and it is enforced by the accumulation of mobile ligand-receptor pairs caused by a vertical pulling force, as suggested by a previous study using artificial model systems and theoretical models (54). By comparing the adhesion contacts on membranes in fluid phase (Fig. 4) and in gel phase (Fig. S5), we experimentally confirmed that the shear-induced pinning near the tip of the cell facing to the flow originates from the lateral accumulation of receptor molecules. Supported membrane systems offer a unique advantage over substrates displaying nanopatterns of receptor molecules because they are capable of fine adjusting not only inter-receptor distance but also membrane fluidity. In this context, it is further worth mentioning that cell-cell adhesion assays support the view of receptor accumulation at contact zones. For example, the engagement of CD36 with infected erythrocytes results in CD36 clustering via a process that involves actin cytoskeleton remodeling and dephosphorylation of Thr[92] in the ectodomain of CD36 (52). Similarly, ICAM-1 molecules can also cluster and are recruited into lipid rafts upon interaction with a ligand (44), in addition to ICAM-1 being upregulated (10- to 20-fold on human brain microvascular endothelial cells and ∼1000-fold on human umbilical vein endothelial cells) in response to inflammatory mediators (49). Other studies have shown that the lifetime of the contact area (containing clusters of ligand-receptor pairs) might be several orders of magnitude higher than the half-life of the single bond dissociation rate (55,56), as dissociated molecules can easily find new interaction partners particularly on substrates with high receptor densities (45). On the basis of these findings, we propose that the same processes as described above occur in vivo and that the shear-induced increases in contact area and tight binding zone contribute to the fact that cytoadhering infected erythrocyte can withstand hydrodynamic pressures of 1.0 Pa and more without peeling off.

The ultrasonic pressure wave assessed the adhesion strength under conditions devoid of nonelastic cell responses. Because of the short interaction time with the pressure wave (full width at half maximum ∼80 ns), the cells are instantaneously detached from the substrates, as all

adhesion bonds are broken simultaneously. Effects occurring under physiological wall shear stress conditions, such as morphological changes due to remodeling of the cytoskeletons (57) and rate-dependent bond rupture forces (56), can therefore be ignored. Thus, the ultrasonic pressure wave assay depicts a more realistic view of the intrinsic adhesion strengths than do standard wash-off experiments using wall shear stresses in the physiological range. Note that the bond rupture force for a receptor-ligand pair depends exponentially on the loading rate (56), which explains the very high cell detachment pressures observed in the ultrasonic pressure wave experiments.

We acknowledge that we cannot attribute the adhesion phenomena described in this study to specific PfEMP1 variants, owing to the fact that the parasite population is heterogeneous with regard to the *var* genes expressed. The generalizability of our findings is also constrained by the range of PfEMP1 variants tested in our infected erythrocyte populations. It is, therefore, speculative to conclude that the PfEMP1-CD36 and the PfEMP1/ICAM-1 interactions behave like slip bonds, although the monotonic decrease in binding events at each $<d>$ with increasing shear stress would be consistent with a slip bond. A catch-slip bond behavior has recently been proposed for the PfEMP1/ICAM-1 interaction, based on single-cell pull experiments conducted using an atomic force microscope (58,59). This observation was made at a very low loading rate, and it is possible that there exists, in the low shear stress regime, a threshold beyond which a catch-slip bond becomes indistinguishable from a slip bond (55). In comparison, the interaction between the PfEMP1 variant VAR2CSA and placental CSA has been described as a cooperative, shear-enhanced catch bond-like behavior (13). It would be interesting to use our system to measure binding characteristics of other PfEMP1-ligand interactions.

Throughout our study, we noted the distinct cytoadhesion characteristics of infected HbAS erythrocytes. Compared with age-matched infected HbAA erythrocytes, the infected sickle cell trait HbAS erythrocytes exhibited two- to fourfold lower adhesion efficiencies on both CD36 and ICAM-1 surfaces at wall shear stresses below 0.05 Pa. At wall shear stresses exceeding 0.05 Pa, the adhesion efficiencies of infected HbAS and HbAA erythrocytes converged. These findings are in line with previous studies showing reduced cytoadhesion of infected HbAS erythrocytes to microvascular endothelial cells under hydrodynamic conditions prevalent in microvenules (8,9,40). The convergence of the adhesion curves is explained by the fact that only 35–45% of total hemoglobin in sickle cell carriers is hemoglobin S (60). It is, therefore, conceivable that blood from sickle cell carriers contains a fraction of wild-type HbAA erythrocytes and that these cells, when infected, adhere under higher wall shear stresses. Along these lines, Cholera et al. reported that a small fraction of infected erythrocytes from patients with the sickle cell trait display knob

sizes and knob density, as well as similar amounts of PfEMP1 on the surface, comparable with parasitized wild-type erythrocytes (8).

The reduced adhesion capability of infected HbAS erythrocytes is also reflected by a 30% smaller contact zones and significantly lower pressures to detach prebound cells. As suggested by both experiments and computer simulations (9,33,40), one of the determinants for the weaker cytoadhesion capacity of infected HbAS erythrocytes is their aberrant knob size and density (5,8,40). Infected HbAS erythrocytes have fewer knobs ($\sigma_{iHbAS} = 3 \pm 2$ knobs μm^{-2}) compared with parasitized HbAA erythrocytes ($\sigma_{iHbAA} = 14 \pm 4$ knobs μm^{-2}). Moreover, the diameter of knobs expressed on iHbAS, $\Phi_{iHbAS} \approx 191 \pm 99$ nm, are larger than those on iHbAA, $\Phi_{iHbAA} \approx 72 \pm 21$ nm (5,6,40). Taking these values, one can calculate a dimensionless knob size $\varepsilon = 2\pi(\Phi/2)^2\sigma$. As expected, this value is higher for infected HbAS erythrocytes ($\sigma_{iHbAS} \sim 0.16$) compared with infected HbAA erythrocytes ($\sigma_{iHbAA} \sim 0.12$). Yet, despite an $\sim 33\%$ smaller dimensionless knob size, the number of PfEMP1 molecules per knob is comparable between both red blood cell types (5), indicating some deeper molecular aberrations, such as impaired export of PfEMP1 molecules and other parasite-encoded factors into the host cell compartment (61), impaired anchoring of PfEMP1 molecules to the membrane skeleton of the host cell via knobs (8,10,62) and/or defects in parasite metabolic activity (63).

In summary, our study supports the use of receptor-functionalized membranes as a complementary tool to study quantitative aspects of cytoadhesion, such as the effect of the receptor distance and mobility on adhesion efficiency. The supported membranes also allowed us to assess the intrinsic binding strengths and to inform on cell-adhesive contact zones and their dynamics under shear stress.

SUPPORTING MATERIAL

AUTHOR CONTRIBUTIONS

ACKNOWLEDGMENTS

SUPPORTING CITATIONS

Reference (64) can be found in the Supporting material.

REFERENCES

1. World Health Organization. 2020. World Malaria Report 2019. WHO Press, Geneva, Switzerland.

2. Smith, J. D., J. A. Rowe, …, T. Lavstsen. 2013. Malaria's deadly grip: cytoadhesion of Plasmodium falciparum-infected erythrocytes. *Cell. Microbiol.* 15:1976–1983.

3. Lee, W. C., B. Russell, and L. Rénia. 2019. Sticking for a cause: the falciparum malaria parasites cytoadherence paradigm. *Front. Immunol.* 10:1444.

4. Wahlgren, M., S. Goel, and R. R. Akhouri. 2017. Variant surface antigens of Plasmodium falciparum and their roles in severe malaria. *Nat. Rev. Microbiol.* 15:479–491.

5. Sanchez, C. P., C. Karathanasis, …, M. Lanzer. 2019. Single-molecule imaging and quantification of the immune-variant adhesin VAR2CSA on knobs of *Plasmodium falciparum*-infected erythrocytes. *Commun. Biol.* 2:172.

6. Fröhlich, B., J. Jäger, …, M. Tanaka. 2019. Hemoglobin S and C affect biomechanical membrane properties of *P. falciparum*-infected erythrocytes. *Commun. Biol.* 2:311.

7. Zhang, Y., C. Huang, …, S. Suresh. 2015. Multiple stiffening effects of nanoscale knobs on human red blood cells infected with Plasmodium falciparum malaria parasite. *Proc. Natl. Acad. Sci. USA.* 112:6068–6073.

8. Cholera, R., N. J. Brittain, …, R. M. Fairhurst. 2008. Impaired cytoadherence of Plasmodium falciparum-infected erythrocytes containing sickle hemoglobin. *Proc. Natl. Acad. Sci. USA.* 105:991–996.

9. Fairhurst, R. M., C. D. Bess, and M. A. Krause. 2012. Abnormal PfEMP1/knob display on Plasmodium falciparum-infected erythrocytes containing hemoglobin variants: fresh insights into malaria pathogenesis and protection. *Microbes Infect.* 14:851–862.

10. Cyrklaff, M., S. Srismith, …, M. Lanzer. 2016. Oxidative insult can induce malaria-protective trait of sickle and fetal erythrocytes. *Nat. Commun.* 7:13401.

11. Sackmann, E. 1996. Supported membranes: scientific and practical applications. *Science.* 271:43–48.

12. Tanaka, M., and E. Sackmann. 2005. Polymer-supported membranes as models of the cell surface. *Nature.* 437:656–663.

13. Rieger, H., H. Y. Yoshikawa, …, M. Lanzer. 2015. Cytoadhesion of Plasmodium falciparum-infected erythrocytes to chondroitin-4-sulfate is cooperative and shear enhanced. *Blood.* 125:383–391.

14. Burk, A. S., C. Monzel, …, A. D. Ho. 2015. Quantifying adhesion mechanisms and dynamics of human hematopoietic stem and progenitor cells. *Sci. Rep.* 5:9370.

15. Gülcüler Balta, G. S., C. Monzel, …, A. Martin-Villalba. 2019. 3D cellular architecture modulates tyrosine kinase activity, thereby switching CD95-mediated apoptosis to survival. *Cell Rep.* 29:2295–2306.e6.

16. Yoshikawa, H. Y., F. F. Rossetti, …, M. Tanaka. 2011. Quantitative evaluation of mechanosensing of cells on dynamically tunable hydrogels. *J. Am. Chem. Soc.* 133:1367–1374.

17. Limozin, L., and K. Sengupta. 2009. Quantitative reflection interference contrast microscopy (RICM) in soft matter and cell adhesion. *ChemPhysChem.* 10:2752–2768.

18. Kaindl, T., H. Rieger, …, M. Tanaka. 2012. Spatio-temporal patterns of pancreatic cancer cells expressing CD44 isoforms on supported membranes displaying hyaluronic acid oligomers arrays. *PLoS One.* 7:e42991.

19. Trager, W., and J. B. Jensen. 2005. Human malaria parasites in continuous culture. 1976. *J. Parasitol.* 91:484–486.

20. Goodyer, I. D., J. Johnson, …, D. J. Hayes. 1994. Purification of mature-stage Plasmodium falciparum by gelatine flotation. *Ann. Trop. Med. Parasitol.* 88:209–211.

21. Claessens, A., and J. A. Rowe. 2012. Selection of Plasmodium falciparum parasites for cytoadhesion to human brain endothelial cells. *J. Vis. Exp* (59):e3122.

22. Uhlemann, A.-C., T. Staalsoe, …, L. Hviid. 2000. Analysis of Plasmodium falciparum-infected red blood cells. *MACS & More.* 4:7–8.

23. Kern, W. 1993. Handbook of Semiconductor Wafer Cleaning Technology. Noyes Publication, New Jersey, pp. 111–196.

24. Körner, A., C. Deichmann, …, M. Tanaka. 2013. Cell differentiation of pluripotent tissue sheets immobilized on supported membranes displaying cadherin-11. *PLoS One.* 8:e54749.

25. Lipowsky, R., and E. Sackmann. 1995. Structure and Dynamics of Membranes: I. From Cells to Vesicles/II. Generic and Specific Interactions. Elsevier, Amsterdam.

26. Yu, L., J. Li, …, L. Liu. 2018. Low cell-matrix adhesion reveals two subtypes of human pluripotent stem cells. *Stem Cell Reports.* 11:142–156.

27. Vogel, A., W. Lauterborn, and R. Timm. 1989. Optical and acoustic investigations of the dynamics of laser-produced cavitation bubbles near a solid boundary. *J. Fluid Mech.* 206:299–338.

28. Plesset, M. S., and R. B. Chapman. 1971. Collapse of an initially spherical vapour cavity in the neighbourhood of a solid boundary. *J. Fluid Mech.* 47:283–290.

29. Gompper, G., T. Ihle, …, R. G. Winkler. 2009. Multi-particle collision dynamics: a particle-based mesoscale simulation approach to the hydrodynamics of complex fluids. *In* Advanced Computer Simulation Approaches for Soft Matter Sciences III C. Holm and K. Kremer, eds.. Springer, pp. 1–87.

30. Noguchi, H., and G. Gompper. 2005. Shape transitions of fluid vesicles and red blood cells in capillary flows. *Proc. Natl. Acad. Sci. USA.* 102:14159–14164.

31. Fedosov, D. A., B. Caswell, and G. E. Karniadakis. 2010. A multiscale red blood cell model with accurate mechanics, rheology, and dynamics. *Biophys. J.* 98:2215–2225.

32. Kikuchi, N., C. M. Pooley, …, J. M. Yeomans. 2003. Transport coefficients of a mesoscopic fluid dynamics model. *J. Chem. Phys.* 119:6388–6395.

33. Waldecker, M., A. K. Dasanna, …, M. Lanzer. 2017. Differential time-dependent volumetric and surface area changes and delayed induction of new permeation pathways in P. falciparum-infected hemoglobinopathic erythrocytes. *Cell. Microbiol.* 19:e12650, Published online August 25, 2016.

34. Suresh, S., J. Spatz, …, T. Seufferlein. 2005. Connections between single-cell biomechanics and human disease states: gastrointestinal cancer and malaria. *Acta Biomater.* 1:15–30.

35. Bell, G. I. 1978. Models for the specific adhesion of cells to cells. *Science.* 200:618–627.

36. Xu, X., A. K. Efremov, …, J. Cao. 2013. Probing the cytoadherence of malaria infected red blood cells under flow. *PLoS One.* 8:e64763.

37. Dasanna, A. K., C. Lansche, …, U. S. Schwarz. 2017. Rolling adhesion of schizont stage malaria-infected red blood cells in shear flow. *Biophys. J.* 112:1908–1919.

38. Korn, C. B., and U. S. Schwarz. 2008. Dynamic states of cells adhering in shear flow: from slipping to rolling. *Phys. Rev. E Stat. Nonlin. Soft Matter Phys.* 77:041904.

39. Lamura, A., and S. Succi. 2005. Lattice mesoscopic model of dynamically heterogeneous fluids. *Phys. Rev. Lett.* 95:224502.

40. Lansche, C., A. K. Dasanna, …, M. Lanzer. 2018. The sickle cell trait affects contact dynamics and endothelial cell activation in *Plasmodium falciparum*-infected erythrocytes. *Commun. Biol.* 1:211.

41. Kraemer, S. M., and J. D. Smith. 2006. A family affair: var genes, PfEMP1 binding, and malaria disease. *Curr. Opin. Microbiol.* 9:374–380.

42. Papaioannou, T. G., and C. Stefanadis. 2005. Vascular wall shear stress: basic principles and methods. *Hellenic J. Cardiol.* 46:9–15.

43. Simson, R., E. Wallraff, …, E. Sackmann. 1998. Membrane bending modulus and adhesion energy of wild-type and mutant cells of Dictyostelium lacking talin or cortexillins. *Biophys. J.* 74:514–522.

44. Tilghman, R. W., and R. L. Hoover. 2002. E-selectin and ICAM-1 are incorporated into detergent-insoluble membrane domains following clustering in endothelial cells. *FEBS Lett.* 525:83–87.

45. Erdmann, T., and U. S. Schwarz. 2004. Stability of adhesion clusters under constant force. *Phys. Rev. Lett.* 92:108102.

46. Tanaka, M., J. Hermann, …, S. G. Boxer. 2007. Frictional drag and electrical manipulation of recombinant proteins in polymer-supported membranes. *Langmuir.* 23:5638–5644.

47. Deng, Y., D. P. Papageorgiou, …, G. E. Karniadakis. 2019. Quantifying shear-induced deformation and detachment of individual adherent sickle red blood cells. *Biophys. J.* 116:360–371.

48. Cooke, B. M., A. R. Berendt, …, G. B. Nash. 1994. Rolling and stationary cytoadhesion of red blood cells parasitized by Plasmodium falciparum: separate roles for ICAM-1, CD36 and thrombospondin. *Br. J. Haematol.* 87:162–170.

49. McCormick, C. J., A. Craig, …, A. R. Berendt. 1997. Intercellular adhesion molecule-1 and CD36 synergize to mediate adherence of Plasmodium falciparum-infected erythrocytes to cultured human microvascular endothelial cells. *J. Clin. Invest.* 100:2521–2529.

50. Yipp, B. G., S. Anand, …, M. Ho. 2000. Synergism of multiple adhesion molecules in mediating cytoadherence of Plasmodium falciparum-infected erythrocytes to microvascular endothelial cells under flow. *Blood.* 96:2292–2298.

51. Yipp, B. G., M. J. Hickey, …, M. Ho. 2007. Differential roles of CD36, ICAM-1, and P-selectin in Plasmodium falciparum cytoadherence in vivo. *Microcirculation.* 14:593–602.

52. Davis, S. P., M. Amrein, …, M. Ho. 2012. Plasmodium falciparum-induced CD36 clustering rapidly strengthens cytoadherence via p130CAS-mediated actin cytoskeletal rearrangement. *FASEB J.* 26:1119–1130.

53. Yipp, B. G., S. M. Robbins, …, M. Ho. 2003. Src-family kinase signaling modulates the adhesion of Plasmodium falciparum on human microvascular endothelium under flow. *Blood.* 101:2850–2857.

54. Smith, A.-S., K. Sengupta, …, E. Sackmann. 2008. Force-induced growth of adhesion domains is controlled by receptor mobility. *Proc. Natl. Acad. Sci. USA.* 105:6906–6911.

55. Evans, E., A. Leung, …, C. Zhu. 2004. Mechanical switching and coupling between two dissociation pathways in a P-selectin adhesion bond. *Proc. Natl. Acad. Sci. USA.* 101:11281–11286.

56. Merkel, R., P. Nassoy, …, E. Evans. 1999. Energy landscapes of receptor-ligand bonds explored with dynamic force spectroscopy. *Nature.* 397:50–53.

57. An, X., M. C. Lecomte, …, W. Gratzer. 2002. Shear-response of the spectrin dimer-tetramer equilibrium in the red blood cell membrane. *J. Biol. Chem.* 277:31796–31800.

58. Lim, Y. B., J. Thingna, …, C. T. Lim. 2020. Temperature-induced catch-slip to slip bond transit in Plasmodium falciparum-infected erythrocytes. *Biophys. J.* 118:105–116.

59. Lim, Y. B., J. Thingna, …, C. T. Lim. 2017. Single molecule and multiple bond characterization of catch bond associated cytoadhesion in malaria. *Sci. Rep.* 7:4208.

60. Turgeon, M. L. 2011. Clinical Hematology: Theory and Procedures, Fifth Edition. Lippincott Williams & Wilkins, Philadelphia, PA.

61. Kilian, N., S. Srismith, …, M. Lanzer. 2015. Hemoglobin S and C affect protein export in Plasmodium falciparum-infected erythrocytes. *Biol. Open.* 4:400–410.

62. Cyrklaff, M., C. P. Sanchez, …, M. Lanzer. 2011. Hemoglobins S and C interfere with actin remodeling in Plasmodium falciparum-infected erythrocytes. *Science.* 334:1283–1286.

63. Fröhlich, B., Y. Yang, …, M. Tanaka. 2020. Nanofocused scanning X-ray fluorescence microscopy revealing an effect of heterozygous hemoglobin S and C on biochemical activities in *Plasmodium falciparum*-infected erythrocytes. *Anal. Chem.* 92:5765–5771.

64. Park, Y., M. Diez-Silva, …, and S. Suresh. 2008. Refractive index maps and membrane dynamics of human red blood cells parasitized by Plasmodium falciparum. *Proc. Natl. Acad. Sci. U S A.* 105:13730–13735.

Supplemental information

Functionalized supported membranes for quantifying adhesion of *P. falciparum*-infected erythrocytes

Benjamin Fröhlich, Anil K. Dasanna, Christine Lansche, Julian Czajor, Cecilia P. Sanchez, Marek Cyrklaff, Akihisa Yamamoto, Alister Craig, Ulrich S. Schwarz, Michael Lanzer, and Motomu Tanaka

Supporting Information to

Functionalized supported membranes for quantifying adhesion of *P. falciparum*-infected erythrocytes

Benjamin Fröhlich[1], Anil K. Dasanna[2†], Christine Lansche[3], Julian Czajor[1], Cecilia P. Sanchez[3],

Marek Cyrklaff[3], Akihisa Yamamoto[4], Alister Craig[5], Ulrich S. Schwarz[2*], Michael Lanzer[3*], and

Motomu Tanaka[1,4*]

[1]Physical Chemistry of Biosystems, Institute of Physical Chemistry, Heidelberg University,
69120 Heidelberg, Germany

[2]Institute for Theoretical Physics and BioQuant-Center for Quantitative Biology, Heidelberg
University, 69120 Heidelberg, Germany

[3]Department of Infectious Diseases, Parasitology, Universitätsklinikum Heidelberg, Im
Neuenheimer Feld 324, 69120 Heidelberg, Germany

[4]Center for Integrative Medicine and Physics, Institute for Advanced Study, Kyoto University,
606-8501 Kyoto, Japan

[5]Liverpool School of Tropical Medicine, Pembroke Place, Liverpool, L3 5QA UK

Corresponding Authors. schwarz@thphys.uni-heidelberg.de, Michael.Lanzer@med.uni-heidelberg.de, and tanaka@uni-heidelberg.de

Present Address. †Institute of Complex Systems, Research Center Juelich, 52425 Juelich, Germany

Supporting Information S1
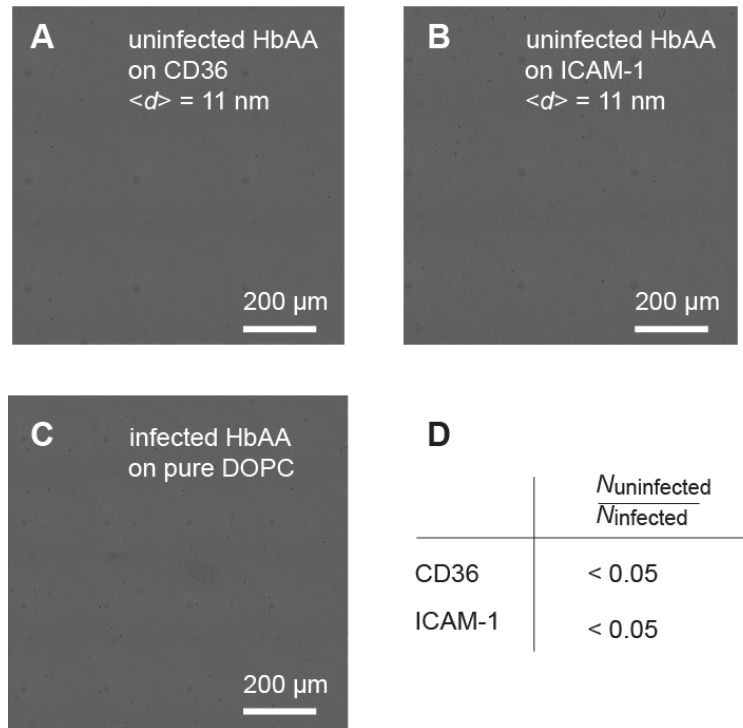
Control experiments for non-specific cytoadhesion

Figure S1. Bright field microscopy images of uninfected HbAA erythrocytes on (A) CD36 and (B) ICAM-1 surfaces with $<d>$ = 11 nm. Panel (C) hsows a bright field image of infected HbAA (trophozoite stage) on pure DOPC membranes. Erythrocytes at a hematocrit of 10^6 cells mL^{-1} were flushed over CD36 or ICAM-1 functionalized membranes for 15 min at a low wall shear stress (τ = 0.03 Pa). The non-specifically adherent cells were removed at τ = 0.8 Pa following our previous report (1). (D) The number of uninfected erythrocytes remaining on the surface $N_{uninfected}$ normalized by that of infected erythrocytes $N_{infected}$ after rinsing (τ = 0.8 Pa) confirmed that adhesion of infected erythrocytes to CD36 and ICAM-1 surfaces is specific. In case of HbAS, we could hardly capture cells on the surface because of weaker adhesion (data not shown).
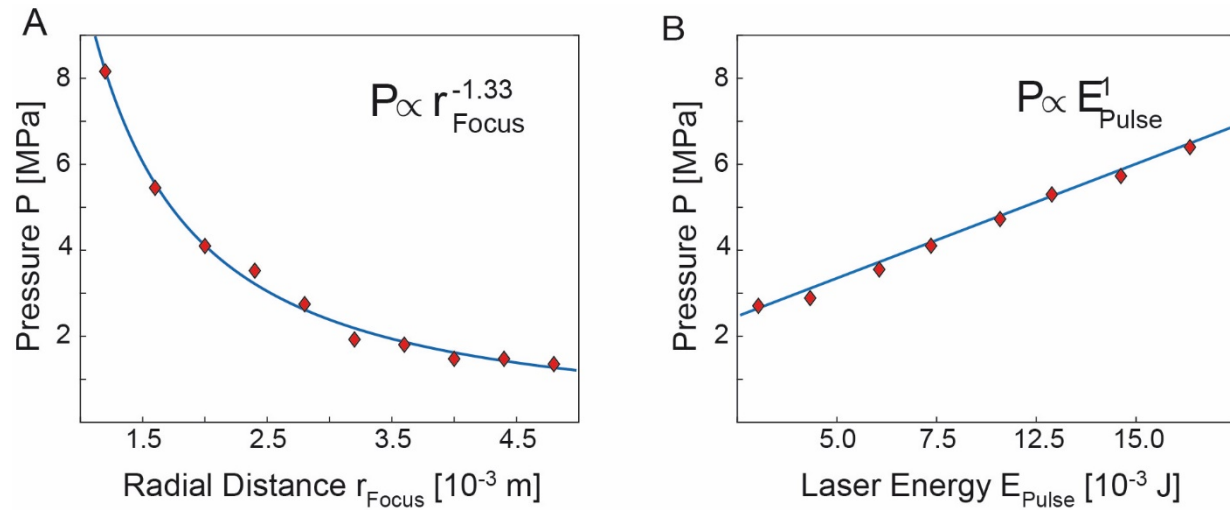
Calibration of pressure using distance and pulse energy

Figure S2. Pressure wave calibration. (A) Pressure P as a function of radial distance from the laser focus point r_{Focus} using a constant laser energy of $E_{pulse} = 7.5$ mJ and the corresponding power law coefficient. (B) Linear dependency of applied pressure P as a function of the laser pulse energy E_{pulse} measured at a constant distance of $r_{Focus} = 2$ mm.

Supporting Information S3

Dependence of critical pressure for cell detachment intermolecular distance.
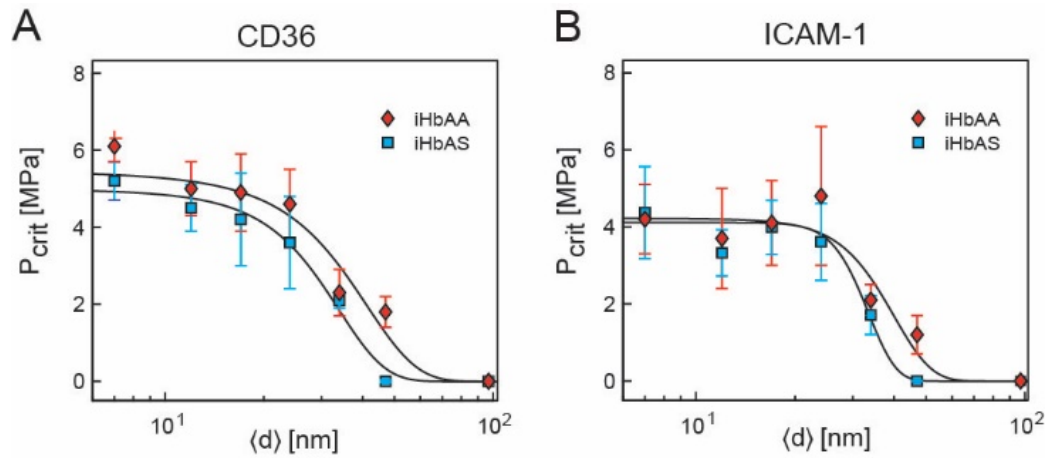
Figure S3. Critical detachment pressures *P** plotted as functions of *<d>* for (A) CD36 (B) and ICAM-1. Red symbols: infected HBAA (iHbAA). Blue symbols: infected HbAS (iHbAS).

Supporting Information S4

Catogorization of "adhesion contact area" and "tight binding zone" (Figure 4)

In a first step, the image sequence was checked for completeness to exclude detached cells or cells with high lateral drift from the analysis. (IV) For each frame the RICM raw image intensity was normalized to the mean intensity level derived from the cell free area applying a background mask:

$$I_{\text{norm}}(x, y, t) = \frac{I(x, y, t)}{\langle I(x, y, t) \rangle_{\text{Bgr}}}$$

The mean contact area or "area of close proximity" was determined from the gradient image of the time averaged intensity image (V). RICM imaging only allows to correctly convert intensity into height, if all layer thicknesses and their respective refractive indices are known. Unfortunately, the cytosolic refractive index is rendered highly inhomogeneous by the infection of *P. falciparum* making it a unknown function of the lateral position x, y (2). (VI) Instead, the mean square amplitude of intensity was derived over all frames:

$$MSA(x, y) = \frac{1}{n_{\text{frames}}} \sum_1^{n_{\text{frames}}} \left(\langle I_{\text{norm}}(x, y, t) \rangle_t - I_{\text{norm}}(x, y, t) \right)^2.$$

(VII) Under the assumption that small changes in intensity ΔI_{norm} scale linearly with changes in height Δh, the intensity mean square amplitude was utilized to define an area of adhesion $A_{Adhesion}$ as:

$$A_{Adhesion} = \sum_{1 \leq x \leq x_{\text{max}}, 1 \leq y \leq y_{\text{max}}}^{MSA(x,y) \leq MSA_T} 1$$

By categorizing a pixel as adherent if the corresponding MSA was below an upper threshold limit MSA$_T$. From adherent cells at high shear stress conditions, we chose MSA$_T$.level at 0.02. In the case of infected erythrocytes, the MSA in the region below the parasite digestive vacuole incorrectly indicated non-adhesion area conditions, since the lateral movement of the heme crystals naturally created large intensity fluctuations. Therefore, pixels inside a manually added circular mask were not subjected to the analysis (c and d, VII). The loss in adhesion area was corrected afterwards under the assumption that the ratio of adhesion to non-adhesion area was homogeneous throughout the cell contact area.
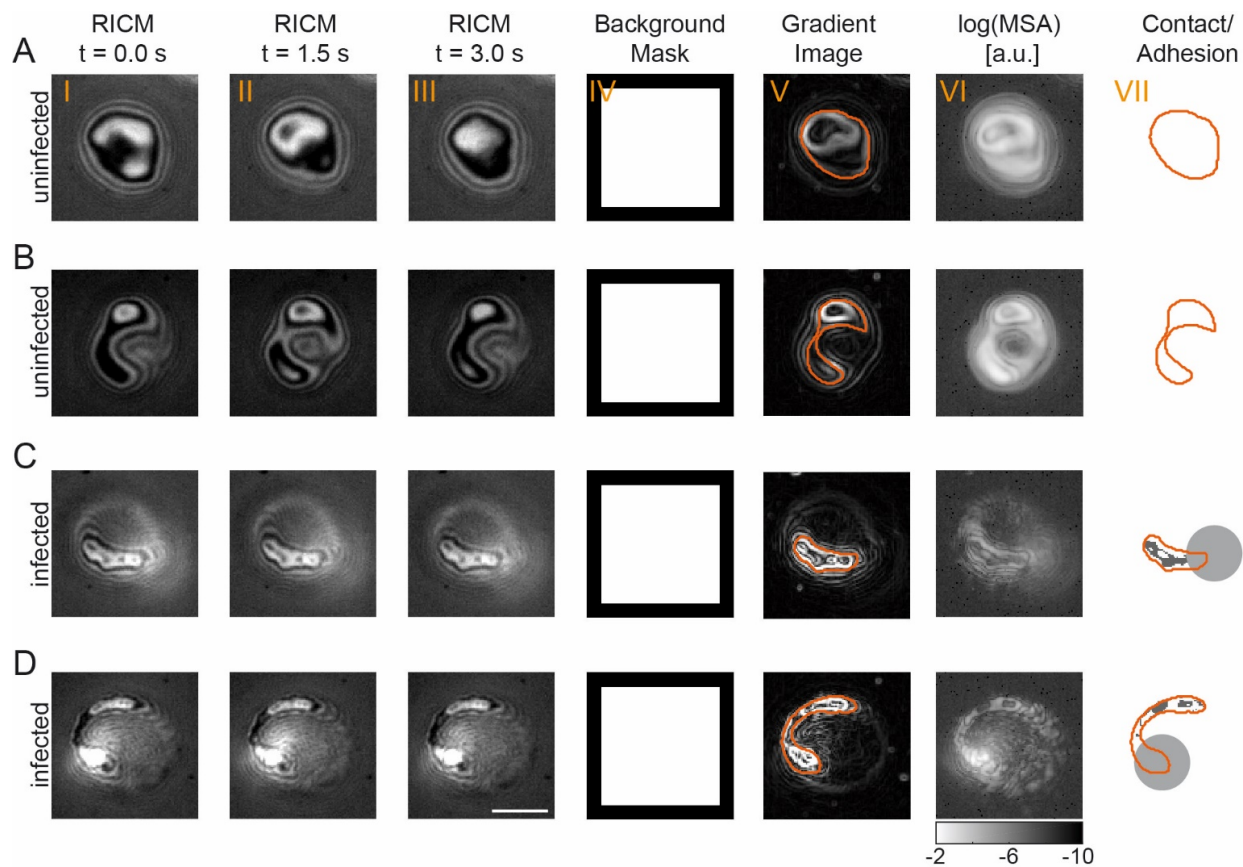

Figure S4. Determination of the contact area and the area of adhesion based on RICM image sequences. (A) and (B) RICM images for different time points (I-III) of uninfected erythrocytes incubated for 30 minutes on a supported bilayer functionalized with CD36 at <d> = 11 nm. Black

region (IV) masks a cell-free background area used to normalize the intensity. (V) The area of close contact (orange line) was derived from the intensity gradient of the time average of the image sequence. (VI) The mean square amplitude (MSA) of the intensity is used to identify the area of adhesion based on the MSD thresholding. (VII) No area of adhesion for uninfected erythrocytes. (C) and (D) analogue procedure for RICM image sequences obtained for infected erythrocytes at trophozoite stage under comparable experimental conditions. (VII) The adhesion area is depicted in dark grey. The influence of the moving haemozoin inside the parasite digestive vacuole was corrected for, manually, using a circular shade (light grey). Scale bar, 4 μm.

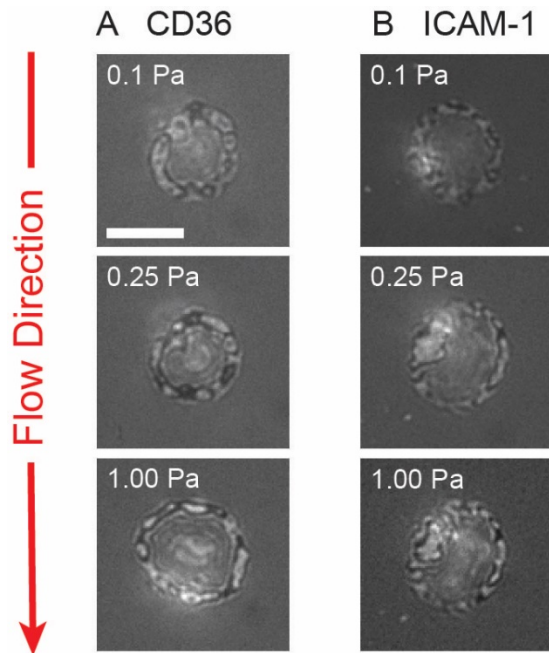**Influence of receptor mobility on shape of adhesion contact**

Figure S5. RICM images of iHbAA erythrocytes on 1,2-palmitoyl-sn-glycero-3-phosphocholine (DPPC) membranes in gel phase displaying (A) CD36 and (B) ICAM-1 at $<d>$ = 11 nm with increasing shear stress. Scale bar: 5 µm. A red arrow indicates the flow direction. Note that the contact area did not take a "raindrop-shape" observed on DOPC membranes in fluid phase at 1.00 Pa (Figure 4), indicating that the pinning of the tip of the cell facing to the flow originates from the shear-induced accumulation of ligand-receptor pairs.

1. Rieger, H., H. Y. Yoshikawa, K. Quadt, M. A. Nielsen, C. P. Sanchez, A. Salanti, M. Tanaka, and M. Lanzer. 2015. Cytoadhesion of Plasmodium falciparum-infected erythrocytes to chondroitin-4-sulfate is cooperative and shear enhanced. Blood 125(2):383-391.
2. Park, Y., M. Diez-Silva, G. Popescu, G. Lykotrafitis, W. Choi, M. S. Feld, and S. Suresh. 2008. Refractive index maps and membrane dynamics of human red blood cells parasitized by Plasmodium falciparum. Proceedings of the National Academy of Sciences 105(37):13730-13735.